

# Synthesis and Optical Properties of Large-Area Single-Crystalline 2D Semiconductor WS<sub>2</sub> Monolayer from Chemical Vapor Deposition

Chunxiao Cong, Jingzhi Shang, Xing Wu, Bingchen Cao, Namphung Peimyo, Caiyu Qiu, Litao Sun, and Ting Yu\*

Being entangled in controlling the electronic properties of graphene for next-generation electronics,<sup>[1,2]</sup> monolayer transition metal dichalcogenides such as MS<sub>2</sub> (M = Mo, W) are attracting great interest as 2D semiconductors with a native direct-energy gap in the visible frequency range.<sup>[3,4]</sup> Monolayers of other layered materials such as *h*-BN, GaS, GaSe, TaSe<sub>2</sub>, and so on, have also attracted much attention because of their unique properties when scaled down to monolayers.<sup>[5–8]</sup> There are comprehensive and intensive studies on monolayer MoS<sub>2</sub>, including its optical and electronic properties,<sup>[9–17]</sup> valleytronics,<sup>[18–21]</sup> strain effects,<sup>[22–24]</sup> thermal effects,<sup>[25]</sup> and so on. However, investigations of WS<sub>2</sub> have just started. Similar to 2H-MoS<sub>2</sub>, monolayer 2H-WS<sub>2</sub> can be constructed by sandwiching two atomic layers of S and one atomic layer of W through covalent W–S bonds, where W locates at the body center of a trigonal-prismatic case formed by six S atoms. Confinement of charge carriers inside the horizontal atomic plane gradually enlarges energy gaps when thinning WS<sub>2</sub> layers.<sup>[26]</sup> Instead of an indirect energy gap for multiple layers, a direct energy gap of ~2 eV at the corners (K and K' points) of the Brillouin Zone could be formed in monolayer WS<sub>2</sub> as clearly demonstrated by both theoretical and experimental studies.<sup>[9,27–29]</sup> The immediate consequence, also a benefit of the existence of such direct bandgap, is the significant enhancement of visible light emission. In WS<sub>2</sub> monolayers,

breaking inversion symmetry leads to the strong spin–orbit coupling and the splitting of valence bands at K/K' points with a sub-gap of around 0.4 eV.<sup>[30]</sup> Furthermore, the split spins at the time-reversed K and K' valleys have the opposite signs. Thus, such spin–valley coupling offers an extra degree of freedom to charge carriers in WS<sub>2</sub> monolayers. Though it has not been reported in monolayer WS<sub>2</sub>, theory predicts and experiments have observed in monolayer MoS<sub>2</sub> a non-equilibrium charge carrier imbalance at two valleys, revealed by the remarkable difference of absorption of left- (σ<sup>−</sup>) and right-handed (σ<sup>+</sup>) circular polarized lights at the two valleys.<sup>[9,18–21,31]</sup> All these interesting and important properties, plus the newly revealed potential in the flexible heterostructures of graphene–WS<sub>2</sub> stacks<sup>[32,33]</sup> guarantee a promising future of WS<sub>2</sub> as the candidate of next-generation nanoelectronics, spintronics, valleytronics, and optoelectronics.<sup>[34]</sup> However, compared to graphene, it is very difficult to prepare MS<sub>2</sub> monolayers, and atomically thin MS<sub>2</sub> flakes made by mechanical exfoliation are much smaller, in fact too small to be well characterized and processed for devices. Most recently, chemical vapor deposition (CVD) has been used to successfully grow large-area single crystals of monolayer MoS<sub>2</sub>.<sup>[11,35–38]</sup> However, the closed count partner—WS<sub>2</sub> single crystalline monolayers—can only be synthesized by CVD with dimensions of a few micrometers. There are other methods such as intercalation or hydrothermal methods which have been used to synthesize WS<sub>2</sub> monolayers.<sup>[39]</sup> In this communication, we report the growth of large-area triangular single crystals of WS<sub>2</sub> monolayer (up to hundreds of micrometers) with high optical quality via a one-step direct sulfurization of WO<sub>3</sub> powders, and we probe their optical properties.

As illustrated in **Figure 1a**, the growth process is very different with the previously reported CVD growth of WS<sub>2</sub> thin flakes.<sup>[40]</sup> Without the pre-deposition of WO<sub>3</sub> thin film in a high-vacuum chamber, in this work, rather than by a two-step process, we fabricate large-area single crystalline WS<sub>2</sub> monolayers by one step: the direct sulfurization of WO<sub>3</sub> powders by sulfur powders at 750 °C (the detailed growth mechanism is proposed below). The substrates used here are well cleaned 300 nm SiO<sub>2</sub>/Si wafers. One SiO<sub>2</sub>/Si substrate is covered with some WO<sub>3</sub> powders with another piece of blank SiO<sub>2</sub>/Si substrate placed face down above it, and this is then heated in a small one-end sealed quartz tube inside a big quartz tube by a tube furnace. **Figure 1b,c**, and **d** present optical microscopy, scanning electron microscopy (SEM), and atomic force microscopy (AFM) images, respectively, of our CVD-grown WS<sub>2</sub> flakes on the substrate. It can be clearly seen that atomically thin flakes with a

Dr. C. X. Cong, J. Z. Shang, B. C. Cao,  
N. Peimyo, Dr. C. Y. Qiu, Prof. T. Yu  
Division of Physics and Applied Physics  
School of Physical and Mathematical Sciences  
Nanyang Technological University  
Singapore, 637371, Singapore  
E-mail: yuting@ntu.edu.sg  
Dr. X. Wu, Prof. L. T. Sun  
SEU-FEI Nano-Pico Center  
Key Laboratory of MEMS of Ministry of Education  
School of Electrical Science and Engineering  
Southeast University  
Nanjing, 210096, China  
Prof. T. Yu  
Department of Physics  
Faculty of Science  
National University of Singapore  
117542, Singapore  
Prof. T. Yu  
Graphene Research Center  
National University of Singapore  
117546, Singapore



DOI: 10.1002/adom.201300428

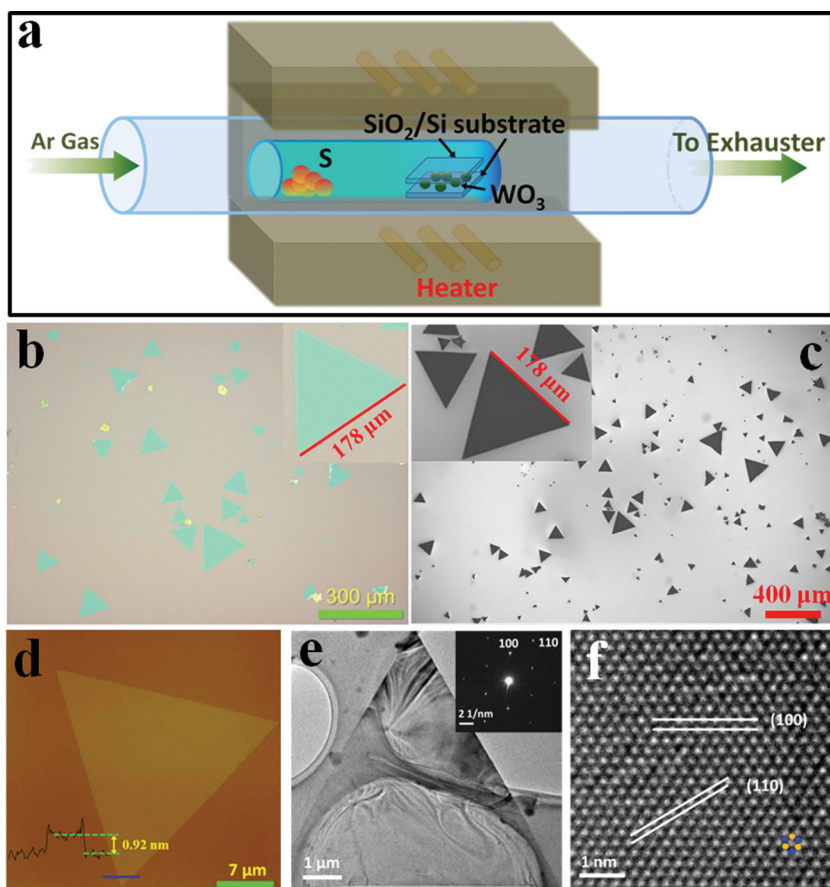


**Figure 1.** (a) Schematic diagram of the CVD system used for the growth of WS<sub>2</sub>. (b) Optical image of as-grown WS<sub>2</sub> on SiO<sub>2</sub> (300 nm)/Si substrate. Inset shows a triangular monolayer WS<sub>2</sub>. (c) SEM image of the area shown in (a). (d) AFM image of a monolayer WS<sub>2</sub>. The height profile demonstrates the as-grown WS<sub>2</sub> flakes are monolayers. (e,f) Low- and high-magnification TEM images of triangular WS<sub>2</sub> monolayer, respectively. Optical, SEM, AFM, and TEM images show the perfect triangular shape and sharp edges (at the microscale) of the as-grown WS<sub>2</sub> monolayers.

perfect triangular shape and sharp edges are effectively formed on the 300 nm SiO<sub>2</sub>/Si substrate through the CVD process. It is noted that, though triangular WS<sub>2</sub> monolayers can be readily formed on both bottom pieces which contain WO<sub>3</sub> powders and on the covering pieces which are blank, the WS<sub>2</sub> monolayers grown on the covering substrates are much cleaner and appear as isolated perfect triangles (Figure 1b,c). This could be due to the existence of WO<sub>3</sub> powders and highly concentrated reaction sources on the bottom substrates (see Supporting Figure S1). Due to the sensitivity to the local environment of the CVD growth, the distribution of dimensions of the triangular crystals is quite wide, from a few to hundreds of micrometers large. The wide distribution of sizes is also observed in the previously reported CVD growth of MoS<sub>2</sub> and WS<sub>2</sub>.<sup>[35,36,40]</sup> The zoomed-in optical, SEM, and AFM images show the clean surface of the WS<sub>2</sub> flakes, which is very different to the MoS<sub>2</sub> and WS<sub>2</sub> thin layers grown by CVD previously,<sup>[36,40]</sup> where impurities or small second or even multiple layers existed on top of the monolayers. The thickness of these triangular crystals is

determined by the height profile of AFM and Raman spectroscopy (discussed later). Figure 1e,f present the transmission electron microscopy (TEM) study of the WS<sub>2</sub> monolayers. As with the optical, SEM, and AFM images, a typical low-magnification TEM image (Figure 1e) visualizes the perfect triangular shape and sharp edges of the as-grown WS<sub>2</sub> monolayers. The high-resolution TEM (HRTEM) image (Figure 1f) reveals the hexagonal ring lattice consisting of alternating tungsten atoms (dark dots) and sulfur (gray dots) atoms as schematically illustrated by the blue and yellow spheres. The TEM data also reveal that the sharp edges are at the microscale perpendicular to the [100] crystal-line direction. Though the microscale edges are along the zigzag direction, it should be noticed that our HRTEM image near the edge shows that the edge is not atomically sharp, which ends up with the triangle-like features of a few nanometers (see Supporting Figure S2). A detailed study at the atomic level is needed. All data unambiguously show that the as-grown triangular WS<sub>2</sub> flakes are monolayer. The large dimension, perfect triangular shape, and clean surface indicate the WS<sub>2</sub> monolayers formed in this work could be a perfect candidate for studying fundamental knowledge and developing practical applications of 2D semiconductors.

Raman spectroscopy has been widely used to study 2D materials, such as the determination of numbers<sup>[41–46]</sup> and stacking sequence<sup>[47–49]</sup> of layers, the external field and molecular doping effects,<sup>[50,51]</sup> and the internal and external strain.<sup>[23,24,52–56]</sup>

Figure 2a shows Raman spectra of the as-grown WS<sub>2</sub> monolayer over a frequency range of 80–650 cm<sup>−1</sup> at room temperature with laser excitation at 532 nm. Fifteen Raman modes of WS<sub>2</sub> are present, as labeled, including the first order modes of LA(M), LA(K), E<sub>2g</sub><sup>1</sup>(Γ), E<sub>2g</sub><sup>1</sup>(M) and A<sub>1g</sub><sup>1</sup>(Γ) the second-order mode of 2LA(M), and some combinational modes. The frequency separation of 62.2 cm<sup>−1</sup> between the E<sub>2g</sub><sup>1</sup>(Γ) and A<sub>1g</sub><sup>1</sup>(Γ)<sup>[40]</sup> and the strong 2LA(M) mode at a laser excitation of 532 nm caused by the double resonance scattering could be the spectral fingerprint of monolayer WS<sub>2</sub>.<sup>[57]</sup> The Raman images (Figure 2b) plotted by extracting the intensity and position of the A<sub>1g</sub><sup>1</sup>(Γ) mode also clearly show the perfect triangular shape and uniform thickness of the as-grown WS<sub>2</sub> monolayers.

Figure 2d presents the fluorescence (FL) image of the as-grown WS<sub>2</sub> monolayers (their optical images are shown in Figure 2c). It can be clearly seen that triangular WS<sub>2</sub> monolayers emit strong red luminescence, resulting from the direct energy gap in such monolayers, and that the intensity of the light emission gradually decays from the edges to the body centers of the triangles. These observations demonstrate that the light emission yield of the CVD WS<sub>2</sub> monolayers is

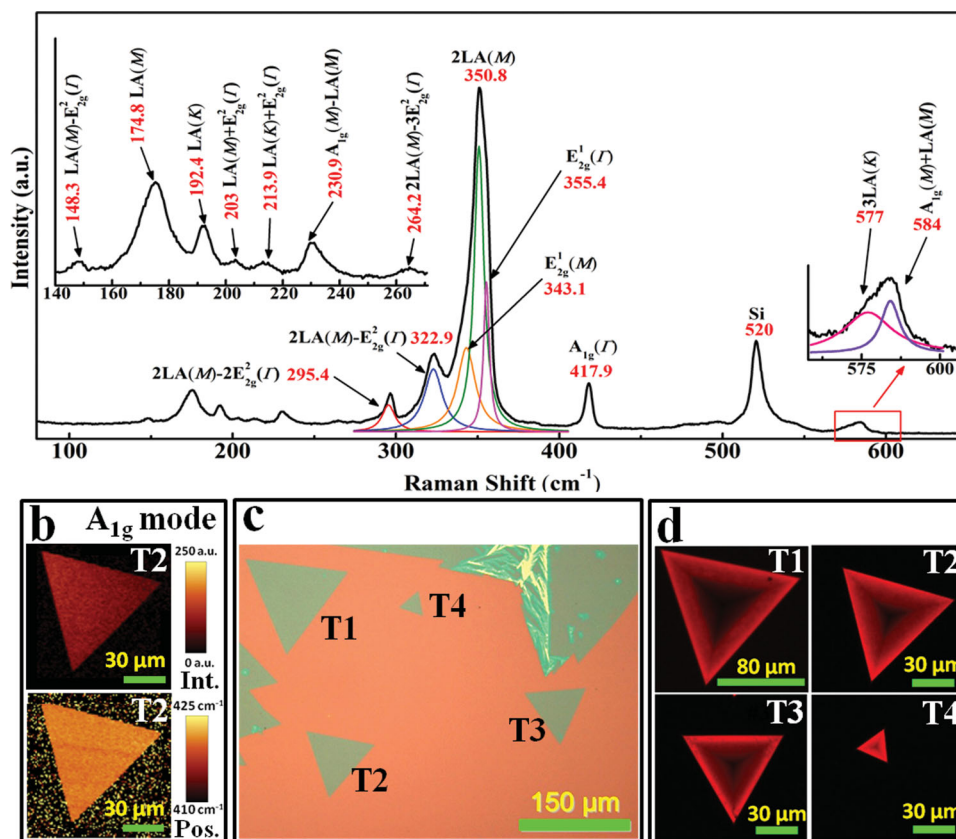


**Figure 2.** (a) Raman spectra of a WS<sub>2</sub> monolayer at room temperature. (b) Raman image of a triangular single crystal of WS<sub>2</sub> monolayer constructed by plotting A<sub>1g</sub> mode intensity (upper panel) and peak position (lower panel). (c) Optical image of as-grown WS<sub>2</sub> on SiO<sub>2</sub> (300 nm)/Si substrate. (d) Fluorescence images of the as-grown WS<sub>2</sub> flakes shown in the optical image of (c).

extremely high and the FL image could be a quick and efficient tool to study such 2D direct energy-gap semiconductors.

To probe the details of light emission from the CVD WS<sub>2</sub> monolayer, micro-photoluminescence (PL) spectroscopy is used and the PL spectra from the edge to the body center are plotted in **Figure 3a**. Not only the intensities, but also the peak position and peak width of the PL vary from the edge to the center. As shown, a blueshift together with quenching of the PL appears from the center relative to that of the edge. To explore this non-uniformity across the monolayer, we conducted PL mapping. **Figure 3b** shows the corresponding PL intensity image of the triangular WS<sub>2</sub> monolayer. As reflected in the FL image, the edges emit the strongest light, and the strength of the emission gradually decays when moving towards the body center, and eventually becomes relatively “dark”. The PL line scanning profiles of the location marked by the lines in **Figure 3b–d** are shown in **Figure S3**, which displays a detailed evolution of PL intensity, peak width, and peak position from the edge to the body. Though there is the reduction of light emission intensity from edges to body center, the overall PL, even from the body of the WS<sub>2</sub> monolayer, is comparable to the PL of the mechanically exfoliated WS<sub>2</sub> (MC-WS<sub>2</sub>) monolayer, and is much stronger than that of the mechanically exfoliated MoS<sub>2</sub> (MC-MoS<sub>2</sub>) monolayer, as shown in **Figure 3f,h,j**. It is noted that samples of even better quality can be formed by controlling the location and heating duration of the sulfur powder. For

example, by heating the sulfur powders loaded at the upstream and outside of the furnace heating zone, WS<sub>2</sub> monolayers with uniform light emission (as strong as the light emitting from MC-WS<sub>2</sub> monolayers) over the entire triangles were obtained (see Supporting Figure S4). It is also noticed that a weak peak located at around 525 nm, around 0.4 eV higher than the dominant A exciton peak, is present in the PL spectrum of the WS<sub>2</sub> monolayer under the excitation laser of 457 nm (see **Figure 3k**), which is the so-called the B exciton emission.<sup>[28,29]</sup> The observation of a B exciton peak, which was not seen in the CVD-grown WS<sub>2</sub> monolayers reported previously,<sup>[40]</sup> further demonstrates the high optical quality of our large-area WS<sub>2</sub> monolayers and strong spin–orbit coupling. Another consequence, also a great benefit of such strong spin–orbit coupling in MS<sub>2</sub> monolayers, is the presence of valley-selective circular dichroism, which offers promising practical potential in valleytronics. Circularly polarized PL is an effective way to probe the valley dependence. Supporting Figure S5 presents the circularly polarized PL spectra of mechanically exfoliated MoS<sub>2</sub> and the CVD-grown WS<sub>2</sub> monolayers under an excitation laser of 633 nm. The incident light is fixed as left-handed circularly polarized, while the emitting light is selectively collected from left- and right-handed circularly polarizations. The net degree of the circular polarization is also plotted. As expected, an obvious valley-selective circular dichroism could be clearly observed in the CVD-grown WS<sub>2</sub> monolayer even at room temperature.



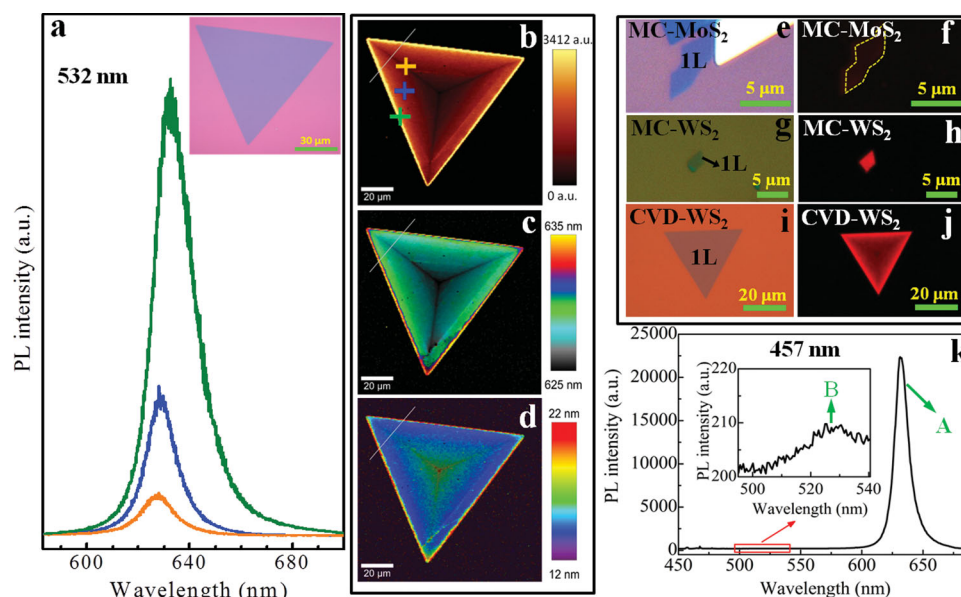


**Figure 3.** (a) PL spectra of the corresponding (colors) points shown in (b). The inset of (a) shows the optical image of the monolayer WS<sub>2</sub> flake studied here. (b–d) PL images of the peak integrated intensity, position, and width, respectively. The lines indicate the locations for the PL line scanning investigation (see Supporting Figure S3). (e,g,i) Optical images of mechanically exfoliated MoS<sub>2</sub> (MC-MoS<sub>2</sub>), and WS<sub>2</sub> (MC-WS<sub>2</sub>) monolayer, and CVD-WS<sub>2</sub> monolayer. (f,h,j) The corresponding fluorescence (FL) images of the samples shown in (e,g,i). The FL images are taken under the identical conditions for MoS<sub>2</sub> and WS<sub>2</sub> monolayer flakes. The bright FL image indicates the ultrahigh quantum yield of direct bandgap light emission from our CVD-grown WS<sub>2</sub> monolayers. (k) PL spectrum of CVD WS<sub>2</sub> monolayer excited by 457 nm laser. The B exciton peak can be clearly seen in the inset.

As predicted and observed, the monolayer WS<sub>2</sub> possesses a direct energy gap of ~2 eV.<sup>[9,27–29]</sup> The strong PL peaks locating at 635 nm for the edges and 625 nm for the center are from the exciton emission. The blueshift and the suppressing of PL at the center might be due to the existence of structural and charged defects, such as S-vacancies, as such a defect may cause *n*-type doping in the WS<sub>2</sub> monolayer.<sup>[58,59]</sup> The sulfurization of WO<sub>3</sub> powders to produce WS<sub>2</sub> nanostructures has been widely adopted.<sup>[40,60]</sup> Recently, a modified two-step CVD process was used to grow nanometer and micrometer WS<sub>2</sub> monolayers on SiO<sub>2</sub>/Si substrates at 800 °C.<sup>[40]</sup> In this work, we developed a CVD process to grow hundreds of micrometer triangular single crystals of WS<sub>2</sub> monolayers on clean and blank 300 nm SiO<sub>2</sub>/Si substrates. In general, WO<sub>3</sub> powders on one SiO<sub>2</sub>/Si substrate together with another piece of covering blank SiO<sub>2</sub>/Si substrate were heated in a small-diameter one-ended sealed quartz tube inside a big-diameter quartz tube by a tube furnace. To sulfurize the WO<sub>3</sub>, sulfur powder was introduced into the upstream part of the quartz tube, where the temperature is around 200–250 °C. Different from the process reported previously,<sup>[40]</sup> we used a one-end sealed inner quartz tube, which was pre-cleaned by isopropyl alcohol (IPA) and deionized water, inside a big quartz tube, which could effectively increase the concentration and pressure of vapor source for growth. During the whole process, argon gas flowed at a rate of 100 sccm. We propose the mechanism of such a CVD process for the growth of large-area WS<sub>2</sub> monolayers as the following: Firstly, flakes of WO<sub>3</sub>S<sub>2-y</sub> were formed. Then, further sulfurization produces triangular shaped thick WS<sub>2+x</sub> flakes with a mixture of W<sub>IV</sub> and W<sub>VI</sub>. As the apex of the triangles could be very active sites for nucleation, a series of triangles formed and merged into a big tri-

angle. With continuous heating, the thick WS<sub>2+x</sub> flakes started expanding and thinning, and eventually WS<sub>2</sub> monolayers were fabricated. The formation of thin layers of WS<sub>2</sub> started at the center of the thick triangles, since there were less overlapping small triangles here and exposure to sulfur for the longest duration. It should be noted that such center areas are also the most exposed regions after the sulfur source is exhausted during the final heating and cooling stages, which may cause a loss of the final sulfur in the monolayers. The whole growth process can be well understood by the images presented in Figure 4. Figure 4a–d is the schematic diagram illustrating the growth of the WS<sub>2</sub> monolayer. Figure 4e–h show optical images of the products at different growth stages, which usually can be simultaneously seen in one substrate, indicating that the growth is very sensitive to the local environment. The formation of WS<sub>2+z</sub> at the thick parts are firmly proven by energy dispersion spectroscopy (EDS) and time of flight secondary ion mass spectrometry (TOF-SIMS) images shown in Supporting Figure S6. The EDS data indicate the ratios of W to S at the thick edge and thin body are 1:2.6 and 1:1.9, respectively. It is well known that W<sub>VI</sub> cannot be directly sulfurized by S unless some intermediates are formed.<sup>[61]</sup> Therefore, we think the transferring of W<sub>VI</sub> to W<sub>IV</sub> at the initial growth stage facilitates the growth of large-area single crystals of WS<sub>2</sub> monolayers under a relatively relaxed condition. A more systematic study of the growth mechanism is ongoing.

We have demonstrated the growth of large-area triangular single crystals of WS<sub>2</sub> monolayers up to hundreds of micrometers in size by chemical vapour deposition through a single step of direct sulfurization of WO<sub>3</sub> powders, and their optical properties have been probed. The observations of high yield of light

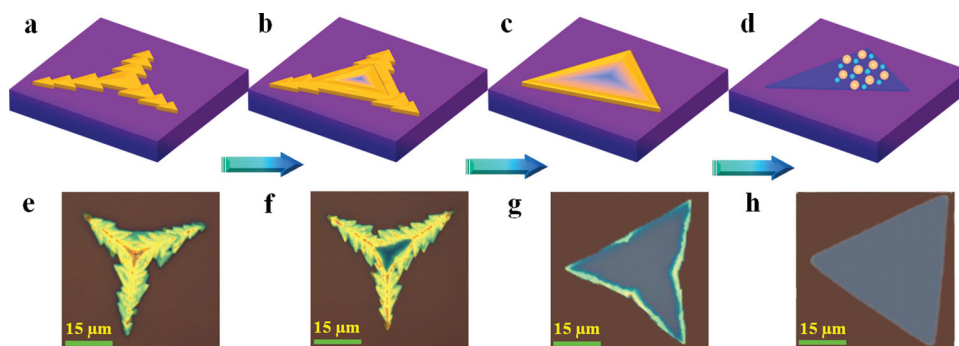


**Figure 4.** (a–d) Schematic diagram illustrates the growth of WS<sub>2</sub> monolayers. (e–h) Optical images of the flakes at the different growth stages. Note: the flakes are not the same piece.

emission and valley-selective circular dichroism provide experimental evidence of the high optical quality of the WS<sub>2</sub> monolayers. This work paves the way to exploit the great potential of WS<sub>2</sub> for future optoelectronics and facilitates fundamental studies of single crystalline 2D transition metal dichalcogenides.

## Experimental Section

**Growth Procedure:** WS<sub>2</sub> monolayer flakes of fine triangular shape were grown by CVD method on well cleaned 300 nm SiO<sub>2</sub>/Si substrates. In general, commercial WO<sub>3</sub> powders (>99.5%, Sigma Aldrich) of 1 mg were spread on one piece of SiO<sub>2</sub>/Si substrate and another piece of blank wafer was placed face-down above (2–3 mm) the bottom piece. They were then loaded into a small diameter quartz tube sealed at one-end which was pre-cleaned by IPA and deionized water. The small diameter quartz tube with 100 mg of sulfur powders (>99.95%, Sigma Aldrich) located at the upstream part of it was introduced inside a big diameter quartz tube heated in a tube furnace. The furnace was heated firstly to 550 °C, then 750 °C with ramping rates of 20 °C/min and 3 °C/min, respectively. After the temperature was kept at 750 °C for 5 min, the furnace was cooled down to room temperature naturally. Ultra-high purity argon gas was flowed with the flowing rate of 100 sccm during the whole growth process.

**Optical and Electronic Microscopy Study:** The PL/Raman mappings/spectroscopies presented in this work were obtained by using a WITec Raman system with a piezocrystal controlled scanning stage. Lasers of 457 nm ( $E_{\text{laser}} = 2.71$  eV), 532 nm ( $E_{\text{laser}} = 2.33$  eV) and 633 nm ( $E_{\text{laser}} = 1.96$  eV) were used as the excitation sources. To avoid heating effect, the laser power at sample surface was controlled below 50 μW. The laser spot size is estimated to be 500 nm. A 100× objective lens with numerical aperture of 0.95 was used for normal PL/Raman measurement. Circularly polarized PL was performed by directing the linearly polarized laser passing through a quarter-wave plate to generate a circularly polarized light. The polarization of the incident light was set to be σ-. The polarization σ- or σ+ of backscattered PL was analyzed by a linear polarizer after the quarter-wave plate. A long-working distance 50× objective lens and a temperature controlled stage HFS600E from Linkam Scientific Instruments were used for circularly polarized PL measurement. The fluorescence images were obtained by an Olympus fluorescence microscope with a Mercury lamp as the excitation light source. The morphologies of as-grown WS<sub>2</sub> monolayer flakes were characterized by field emission scanning electron microscopy (FE-SEM, JEOL JSM-6700F). High-resolution TEM was carried out using an image aberration-corrected TEM system (FEI Titan 80–300). An acceleration voltage of 80 kV was chosen to achieve enough resolution while maintaining the structure of WS<sub>2</sub>.

**EDS and TOF-SIMS:** TOF-SIMS study of the as-grown WS<sub>2</sub> monolayer flakes on SiO<sub>2</sub>/Si substrate was performed on TOF-SIMS<sup>5</sup> (ION-TOF

GmbH) using 50 KeV Bi<sub>3</sub><sup>++</sup> as ion beam. The lateral resolution for SIMS imaging is 100 nm. EDS measurements were carried out using an Energy-dispersive X-ray analysis (EDX, Oxford Instruments) integrated with a Carl Zeiss Auriga system. 80 mm silicon-drift detector enables rapid determination of elemental compositions and acquisition of compositional maps.

## Supporting Information

Supporting Information is available from the Wiley Online Library or from the author.

## Acknowledgements

This work is supported by the Singapore National Research Foundation under NRF RF Award No. NRFRF2010-07 and MOE Tier 2 MOE2012-T2-2-049. C.X. Cong and T. Yu thank WinTech for their help in the TOF-SIMS analysis. X. Wu and L.T. Sun are grateful for the support of Jiangsu Province Funds (No. BK2012024) and Chinese postdoctoral funding (No. 2012M520053).

Received: October 16, 2013

Revised: November 27, 2013

Published online: December 11, 2013

- [1] K. S. Novoselov, A. K. Geim, S. V. Morozov, D. Jiang, Y. Zhang, S. V. Dubonos, I. V. Grigorieva, A. A. Firsov, *Science* **2004**, 306, 666.
- [2] J. van den Brink, *Nat. Mater.* **2010**, 9, 291.
- [3] M. Chhowalla, H. S. Shin, G. Eda, L.-J. Li, K. P. Loh, H. Zhang, *Nat. Chem.* **2013**, 5, 263.
- [4] Q. H. Wang, K. Kalantar-Zadeh, A. Kis, J. N. Coleman, M. S. Strano, *Nat. Nanotechnol.* **2012**, 7, 699.
- [5] R. V. Gorbachev, I. Riaz, R. R. Nair, R. Jalil, L. Britnell, B. D. Belle, E. W. Hill, K. S. Novoselov, K. Watanabe, T. Taniguchi, A. K. Geim, P. Blake, *Small* **2011**, 7, 465.
- [6] L. Lindsay, D. A. Broido, *Phys. Rev. B* **2011**, 84, 155421.
- [7] D. J. Late, B. Liu, J. J. Luo, A. M. Yan, H. S. S. R. Matte, M. Grayson, C. N. R. Rao, V. P. Dravid, *Adv. Mater.* **2012**, 24, 3549.
- [8] P. Hajiyev, C. X. Cong, C. Y. Qiu, T. Yu, *Sci. Rep.* **2013**, 3, 2593.
- [9] A. Splendiani, L. Sun, Y. Zhang, T. Li, J. Kim, C.-Y. Chim, G. Galli, F. Wang, *Nano Lett.* **2010**, 10, 1271.
- [10] K. F. Mak, C. Lee, J. Hone, J. Shan, T. F. Heinz, *Phys. Rev. Lett.* **2010**, 105, 136805.

- [11] A. M. van der Zande, P. Y. Huang, D. A. Chenet, T. C. Berkelbach, Y. M. You, G.-H. Lee, T. F. Heinz, D. R. Reichman, D. A. Muller, J. C. Hone, *Nat. Mater.* **2013**, *12*, 554.
- [12] B. Radisavljevic, A. Radenovic, J. Brivio, V. Giacometti, A. Kis, *Nat. Nanotechnol.* **2011**, *6*, 147.
- [13] G. Eda, H. Yamaguchi, D. Voiry, T. Fujita, M. Chen, M. Chhowalla, *Nano Lett.* **2011**, *11*, 5111.
- [14] D. J. Late, B. Liu, H. S. S. R. Matte, V. P. Dravid, C. N. R. Rao, *ACS Nano* **2012**, *6*, 5635.
- [15] D. J. Late, Y. K. Huang, B. Liu, J. Acharya, S. N. Shirodkar, J. J. Luo, A. M. Yan, D. Charles, U. Waghmare, V. P. Dravid, C. N. R. Rao, *ACS Nano* **2012**, *6*, 5635.
- [16] R. V. Kashid, D. J. Late, S. S. Chou, Y. K. Huang, M. De, D. S. Joag, M. A. More, V. P. Dravid, *Small* **2013**, *9*, 2730.
- [17] D. Jariwala, V. K. Sangwan, D. J. Late, J. E. Johns, V. P. Dravid, T. J. Marks, L. J. Lauhon, M. C. Hersam, *Appl. Phys. Lett.* **2013**, *102*, 173107.
- [18] K. F. Mak, K. L. He, J. Shan, T. F. Heinz, *Nat. Nanotechnol.* **2012**, *7*, 494.
- [19] T. Cao, G. Wang, W. Han, H. Ye, C. Zhu, J. Shi, Q. Niu, P. Tan, E. Wang, B. Liu, J. Feng, *Nat. Commun.* **2012**, *3*, 887.
- [20] D. Xiao, G. B. Liu, W. X. Feng, X. D. Xu, W. Yao, *Phys. Rev. Lett.* **2012**, *108*, 196802.
- [21] G. Sallen, L. Bouet, X. Marie, G. Wang, C. R. Zhu, W. P. Han, Y. Lu, P. H. Tan, T. Amand, B. L. Liu, B. Urbaszek, *Phys. Rev. B* **2012**, *86*, 081301(R).
- [22] J. Feng, X. F. Qian, C. W. Huang, J. Li, *Nat. Photonics* **2012**, *6*, 865.
- [23] Y. Wang, C. Cong, C. Qiu, T. Yu, *Small* **2013**, *9*, 2857.
- [24] C. Rice, R. J. Young, R. Zan, U. Bangert, D. Wolfson, T. Georgiou, R. Jalil, K. S. Novoselov, *Phys. Rev. B* **2013**, *87*, 081307(R).
- [25] S. Najmaei, Z. Liu, P. M. Ajayan, J. Lou, *Appl. Phys. Lett.* **2012**, *100*, 013106.
- [26] R. A. Neville, B. L. Evans, *Phys. Status Solidi B* **1976**, *73*, 597.
- [27] Y. D. Ma, Y. Dai, M. Guo, C. Niu, J. Lu, B. Huang, *Phys. Chem. Chem. Phys.* **2011**, *13*, 15546.
- [28] G. L. Frey, R. Tenne, M. J. Matthews, M. S. Dresselhaus, G. Dresselhaus, *J. Mater. Res.* **1998**, *13*, 2412.
- [29] C. Ballif, M. Regula, P. E. Schmid, M. Remškar, R. Sanjinés, F. Lévy, *Appl. Phys. A-Mater.* **1996**, *62*, 543.
- [30] H. L. Zeng, G.-B. Liu, J. Dai, Y. Yan, B. Zhu, R. He, L. Xie, S. Xu, X. Chen, W. Yao, X. Cui, *Sci. Rep.* **2013**, *3*, 1608.
- [31] H. L. Zeng, J. F. Dai, W. Yao, D. Xiao, X. D. Cui, *Nat. Nanotechnol.* **2012**, *7*, 490.
- [32] L. Britnell, R. M. Ribeiro, A. Eckmann, R. Jalil, B. D. Belle, A. Mishchenko, Y.-J. Kim, R. V. Gorbachev, T. Georgiou, S. V. Morozov, A. N. Grigorenko, A. K. Geim, C. Casiraghi, A. H. Castro Neto, K. S. Novoselov, *Science* **2013**, *340*, 1311.
- [33] T. Georgiou, R. Jalil, B. D. Belle, L. Britnell, R. V. Gorbachev, S. V. Morozov, Y.-J. Kim, A. Gholinia, S. J. Haigh, O. Makarovskiy, L. Eaves, L. A. Ponomarenko, A. K. Geim, K. S. Novoselov, A. Mishchenko, *Nat. Nanotechnol.* **2013**, *8*, 100.
- [34] N. Perea-López, A. L. Elías, A. Berkdemir, A. Castro-Beltrán, H. R. Gutiérrez, S. Feng, R. Lv, T. Hayashi, F. López-Urías, S. Ghosh, B. Muchharla, S. Talapatra, H. Terrones, M. Terrones, *Adv. Funct. Mater.* **2013**, *23*, 200760.
- [35] S. Wu, C. Huang, G. Aivazian, J. S. Ross, D. H. Cobden, X. Xu, *ACS Nano* **2013**, *7*, 2768.
- [36] S. Najmaei, Z. Liu, W. Zhou, X. Zou, G. Shi, S. Lei, B. I. Yakobson, J.-C. Idrobo, P. M. Ajayan, J. Lou, *Nat. Mater.* **2013**, *12*, 754.
- [37] Y. H. Lee, X. Q. Zhang, W. Zhang, M. T. Chang, C. T. Lin, K. D. Chang, Y. C. Yu, J. T. W. Wang, C. S. Chang, L. J. Li, T. W. Lin, *Adv. Mater.* **2012**, *24*, 2320.
- [38] K. K. Liu, W. Zhang, Y. H. Lee, Y. C. Lin, M. T. Chang, C. Y. Su, C. S. Chang, H. Li, Y. Shi, H. Zhang, C. S. Lai, L. J. Li, *Nano Lett.* **2012**, *12*, 1538.
- [39] H. S. S. R. Matte, A. Gomathi, A. K. Manna, D. J. Late, R. Datta, S. K. Pati, C. N. R. Rao, *Angew Chem Int Edit* **2010**, *49*, 4059.
- [40] H. R. Gutiérrez, N. Perea-López, A. L. Elías, A. Berkdemir, B. Wang, R. Lv, F. López-Urías, V. H. Crespi, H. Terrones, M. Terrones, *Nano Lett.* **2013**, *13*, 3447.
- [41] A. C. Ferrari, J. C. Meyer, V. Scardaci, C. Casiraghi, M. Lazzeri, F. Mauri, S. Piscanec, D. Jiang, K. S. Novoselov, S. Roth, A. K. Geim, *Phys. Rev. Lett.* **2006**, *97*, 187401.
- [42] S. L. Li, H. Miyazaki, H. Song, H. Kuramochi, S. Nakaharai, K. Tsukagoshi, *ACS Nano* **2012**, *6*, 7381.
- [43] C. Lee, H. Yan, L. E. Brus, T. F. Heinz, J. Hone, S. Ryu, *ACS Nano* **2010**, *4*, 2695.
- [44] W. Zhao, Z. Ghorannevis, L. Chu, M. Toh, C. Kloc, P.-H. Tan, G. Eda, *ACS Nano* **2013**, *7*, 791.
- [45] S. L. Li, H. M. Wang, J. Kasim, H. M. Fan, T. Yu, Y. H. Wu, Y. P. Feng, Z. X. Shen, *Nano Lett.* **2007**, *7*, 2758.
- [46] D. J. Late, B. Liu, H. S. S. R. Matte, C. N. R. Rao, V. P. Dravid, *Adv. Funct. Mater.* **2012**, *22*, 1894.
- [47] C. H. Lui, Z. Li, Z. Chen, P. V. Klimov, L. E. Brus, T. F. Heinz, *Nano Lett.* **2011**, *11*, 164.
- [48] C. X. Cong, T. Yu, R. Saito, G. F. Dresselhaus, M. S. Dresselhaus, *ACS Nano* **2011**, *5*, 1600.
- [49] C. X. Cong, T. Yu, H. M. Wang, *ACS Nano* **2010**, *4*, 3175.
- [50] B. Chakraborty, A. Bera, D. V. S. Muthu, S. Bhowmick, U. V. Waghmare, A. K. Sood, *Phys. Rev. B* **2012**, *85*, 161403(R).
- [51] S. Tongay, J. Zhou, C. Ataca, J. Liu, J. S. Kang, T. S. Matthews, L. You, J. Li, J. C. Grossman, J. Wu, *Nano Lett.* **2013**, *13*, 2831.
- [52] T. Yu, Z. Ni, C. Du, Y. You, Y. Wang, Z. Shen, *J. Phys. Chem. C* **2008**, *112*, 12602.
- [53] M. Huang, H. Yan, C. Chen, D. Song, T. F. Heinz, J. Hone, *Proc. Natl. Acad. Sci. USA* **2009**, *106*, 7304.
- [54] C. W. Huang, R. J. Shiue, H. C. Chui, W. H. Wang, J. K. Wang, Y. Tzengce, C. Y. Liu, *Nanoscale* **2013**, *10.1039/C3NR00123G*.
- [55] T. M. G. Mohiuddin, A. Lombardo, R. R. Nair, A. Bonetti, G. Savini, R. Jalil, N. Bonini, D. M. Basko, C. Galiotis, N. Marzari, K. S. Novoselov, A. K. Geim, A. C. Ferrari, *Phys. Rev. B* **2009**, *79*, 205433.
- [56] Z. H. Ni, T. Yu, Y. H. Lu, Y. Y. Wang, Y. P. Feng, Z. X. Shen, *ACS Nano* **2008**, *2*, 2301.
- [57] A. Berkdemir, H. R. Gutiérrez, A. R. Botello-Méndez, N. Perea-López, A. L. Elías, C.-I. Chia, B. Wang, V. H. Crespi, F. López-Urías, J.-C. Charlier, H. Terrones, M. Terrones, *Sci. Rep.* **2013**, *3*, 1755.
- [58] W. Zhou, X. Zou, S. Najmaei, Z. Liu, Y. Shi, J. Kong, J. Lou, P. M. Ajayan, B. I. Yakobson, J.-C. Idrobo, *Nano Lett.* **2013**, *13*, 2615.
- [59] K. F. Mak, K. He, C. Lee, G. H. Lee, J. Hone, T. F. Heinz, J. Shan, *Nat. Mater.* **2013**, *12*, 207.
- [60] R. Tenne, L. Margulis, M. Genut, G. Hodes, *Nature* **1992**, *360*, 444.
- [61] A. J. van der Vlies, G. Kishan, J. W. Niemantsverdriet, R. Prins, T. Weber, *J. Phys. Chem. B* **2002**, *106*, 3449.